Valley contrasting bulk photovoltaic effect in a $\mathcal{PT}$-symmetric MnPSe₃ monolayer

Qianqian Xue, Xingchi Mu, Yan Sun, and Jian Zhou ⓘ*

Center for Alloy Innovation and Design, State Key Laboratory for Mechanical Behavior of Materials, Xi'an Jiaotong University, Xi'an 710049, China

Valleytronics, which uses the inequivalent electronic states at the band extrema in semiconductors, has been considered to play a vital role in the future information read/write technology. In this paper, we show that a sizable valley contrasting bulk photovoltaic (BPV) effect could exist even when the total BPV photocurrent component is symmetrically forbidden. We illustrate this argument by using a prototypical two-dimensional (2D) antiferromagnetic (AFM) semiconductor, MnPSe₃ monolayer, that is $\mathcal{PT}$ symmetric ($\mathcal{P}$ and $\mathcal{T}$ refer to spatial inversion and time-reversal operators, respectively). We show that the Néel vector controls the magnetic point group well, so that the BPV current direction can be altered. In this material, the mirror reflection constrains some BPV components to be symmetrically forbidden. Nonetheless, we show that the local symmetry at the valleys allows finite BPV photocurrent components correspondingly. This would lead to hidden valley-polarized photoconductivity, reaching a magnitude of $\sim 300\,\mu A/V^2$, observable experimentally. We further predict that the MnPSe₃ monolayer is an example of a 2D ferrotoroidic system, also depending on the Néel vector direction, which can be characterized via magnetoelectric response measurements. Hence, we provide an exemplary platform for paving the route to future optospintronic and optovalleytronic devices in a single AFM material.

I. INTRODUCTION

Manipulation and control of the electronic state at band extrema near the Fermi energy, known as the band valleys, have received tremendous attention during the past decade [1–5]. Different valleys in semiconductors usually locate in the momentum space with a large separation, guaranteeing their robustness against smooth geometric deformation and low-energy phonon excitations. Valleytronics, which uses valley degree of freedom to constitute the binary logic states (like the charge and spin in electronics and spintronics, respectively), holds the potential for ultrafast and efficient information and data read/write applications [6–9]. Even though early studies on electronic valleys mainly focused on silicon (dating back to the 1970s) [10,11], recently discovered two-dimensional (2D) lattices have significantly promoted their advances [3,12–18]. Currently, to detect the valleytronic feature [19–21], one usually uses an optical absorption spectrum such as circular or linear dichroism spectroscopy [22–24] and electrical approaches such as (quantum) valley Hall effect [14,25–29]. Note that the electric signal is realistic and facile for nanoelectronic devices, yet the Hall effect measurement requires depositing electrodes onto samples, which may introduce unwanted impurities or disorders, and the contacting resistance at the boundary between the electrodes and materials needs to be considered.

In this paper, we propose another valley-contrasting feature that is stimulated by noncontacting optical illumination and can be measured and probed electrically. We discuss such optoelectronic responses via the bulk photovoltaic (BPV) effect

[30] in 2D antiferromagnetic (AFM) honeycomb materials [31]. The AFM systems that compose compensated spin polarization are found to be advantageous due to the absence of a stray field and ultrafast spin dynamics [32]. Hence, they give rise to large information storage density and high switching kinetics in real operations. We apply group theory analysis and conduct first-principles density functional theory (DFT) calculations to show that a valley-contrasting BPV photocurrent could exist in a prototypical AFM MnPSe₃ monolayer. The MnPSe₃ belongs to the 2D transition metal phosphorus trichalcogenides family, usually denoted as $TMPX_3$ ($TM =$ Cr, Mn, Fe, Co, and Ni; and $X =$ S and Se). Depending on the transition metal species, this series of materials exhibits different magnetic patterns. Among them, the MnPSe₃ monolayer shows Néel-type AFM configuration [33], which is $\mathcal{PT}$ symmetric ($\mathcal{P}$ refers to inversion symmetry and $\mathcal{T}$ denotes time-reversal symmetry). As both $\mathcal{P}$ and $\mathcal{T}$ are broken, it holds nondegenerate valley energy levels [34]. Previous nonlinear optics theory has demonstrated that the BPV current under linearly polarized light (LPL) irradiation exhibits a magnetic injection current (MIC) feature [35]. Our calculation suggests a sizable MIC density (one-dimensional current density on the order of 0.01–0.1 A/cm) could emerge under an intermediate light intensity (electric field component on the order of 0.1 MV/cm). In addition, we show that the AFM Néel vector $\mathbf{L}(= \mathbf{M}_{Mn1} - \mathbf{M}_{Mn2}$, Mn1 and Mn2 denote the two Mn sites in the unit cell) could effectively tune the symmetry constraints for the MIC generation. Geometrically, the MnPSe₃ monolayer contains a vertical mirror reflection ($\mathcal{M}$) that constrains some BPV photoconductivity components to be symmetrically forbidden. Nonetheless, the local little group at the two valleys resulting in sizable valley-dependent BPV components shows a hidden valley contrasting feature. This suggests ubiquitous

*jianzhou@xjtu.edu.cn
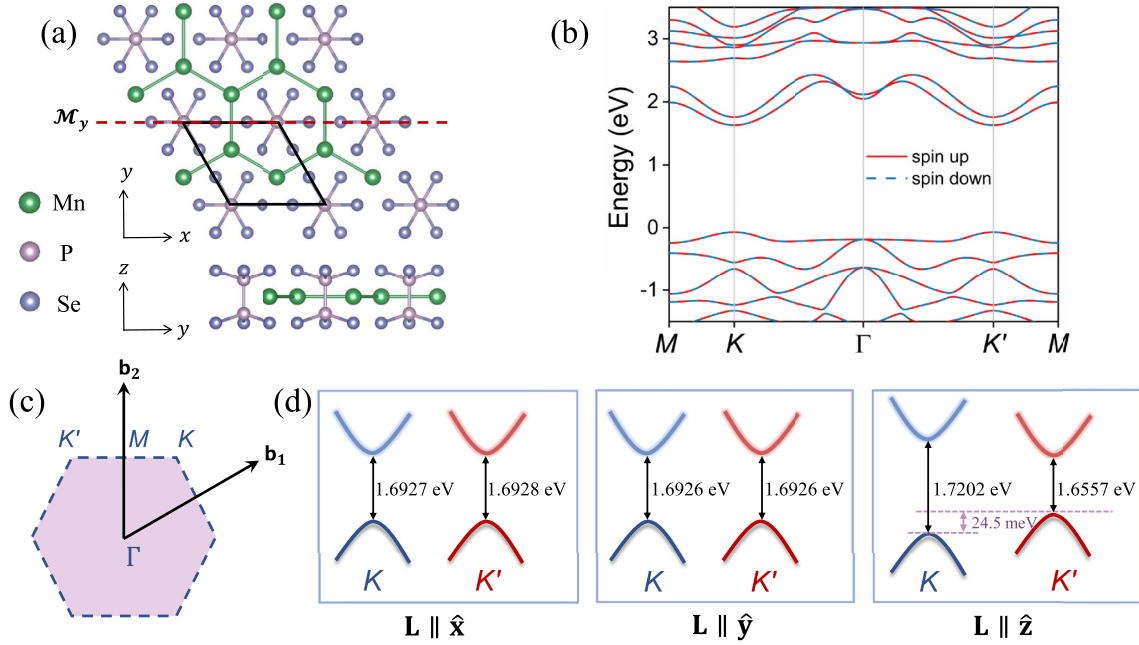
FIG. 1. (a) Top and side views of the MnPSe$_3$ monolayer. The crystalline mirror reflection $\mathcal{M}_y$ is indicated by the horizontal dashed line, and the black rhombus represents the unit cell. (b) Band dispersion along the high-symmetric **k**-path without including spin-orbit coupling (SOC) effect. (c) The first Brillouin zone (BZ), with high-symmetric points of $\Gamma = (0, 0, 0)$, $K = (\frac{1}{3}, \frac{1}{3}, 0)$, $M = (0, \frac{1}{2}, 0)$, and $K' = (-\frac{1}{3}, \frac{2}{3}, 0)$ in direct coordinates. (d) Schematic plots of band edge positions with band gap values when the Néel vector **L** is along the x, y, and z axes with SOC included. Note that each band is doubly degenerate due to antiunitary $\mathcal{PT}$ symmetry.

valley-contrasting MIC in the AFM MnPSe$_3$ monolayer. In addition, we show that the Néel vector **L** strongly couples to the in-plane mechanical deformation, i.e., the in-plane magnetocrystalline anisotropy energy (MAE) can be manipulated via small uniaxial strains. Finally, we suggest that the MnPSe$_3$ monolayer also hosts an **L**-dependent toroidal moment that can be measured by magnetoelectric responses, showing magnetically harnessed ferrotoroidicity.

II. COMPUTATIONAL DETAILS

Our DFT calculations are performed in VASP [36,37], which uses the generalized gradient approximation method in the solid-state Perdew-Burke-Ernzerhof [38] form to treat the exchange-correlation interaction. The projector augmented-wave [39] method is used to describe the core electrons, while the valence electrons are expanded by a plane-wave basis set with its kinetic cutoff energy set to 400 eV. The first Brillouin zone (BZ) is represented by $(12 \times 12 \times 1)$ Monkhorst-Pack **k**-mesh grids [40], and the strong correlation on the Mn-d orbital is treated by adding a Hubbard U correction [41,42] with an effective value of 5 eV. This has been widely adopted in previous works [33], and we note that the exact U value does not affect our main conclusion. If not indicated explicitly, spin-orbit coupling (SOC) is included self-consistently in all our calculations. To simulate 2D materials in the periodic boundary condition, we add a vacuum space of over 20 Å in the out-of-plane z direction, which could eliminate the nearest-neighbor image layer interactions. The convergence criteria of total energy and Hellman-Feynman force components are set as 1×10^{-7} eV and 1×10^{-3} eV/Å, respectively. We fit the DFT-calculated electronic states by using

maximally localized Wannier functions based on Mn-s and d, P-p, and Se-p orbitals, as implemented in the WANNIER90 code [43,44], which are used to evaluate the BPV photoconductivity and magnetoelectric coupling components in our home-built code.

III. RESULTS

A. Geometric, electronic structure, and symmetry arguments

The atomic structure of the MnPSe$_3$ monolayer is plotted in Fig. 1(a). Geometrically, each P dimer is vertically sandwiched by six Se atoms. These P$_2$Se$_6$ moieties are embedded in the hollow sites of the Mn honeycomb sublattice framework. Without considering spin polarization, it belongs to the $P\bar{3}1m$ layer group ($\bar{3}m$ point group), which contains C_{3z} rotation, C_{2y} rotation, and a mirror reflection $\mathcal{M}_y$. Hence, the inversion symmetry $\mathcal{P}$ is also preserved. The Néel-type AFM configuration guarantees the unit cell to be a hexagonal lattice [the black rhombus in Fig. 1(a)], containing two Mn sites that carry antiparallel spin polarization. Before including SOC, the electronic states in the two spin channels (majority and minority) are degenerate [Fig. 1(b)], with the valence and conduction band valleys locating at the corner of the first BZ (K and K' points). The direct band gap value is calculated to be 1.697 eV, consistent with previous reports [31].

The inclusion of SOC breaks the spin-rotational symmetry. In this case, the system becomes $\mathcal{PT}$ preserved, so that each band is still doubly degenerated due to its antiunitary symmetry. Since the spin angular momentum transforms as a pseudovector, its direction would determine the magnetic point group and the valley splitting. We list the basic

TABLE I. Magnetic point group, mirror reflection, and relative energies for **L** along three Cartesian axes.

Néel vector	Magnetic point group at Γ	Mirror reflection	Relative energy (μeV per unit cell)
L ∥ $\hat{\mathbf{x}}$	$2'/m$	$\mathcal{M}_y$	0
L ∥ $\hat{\mathbf{y}}$	$2/m'$	$\mathcal{M}_y\mathcal{T}$	1.63
L ∥ $\hat{\mathbf{z}}$	$\bar{3}'m$	$\mathcal{M}_y$	494

symmetric arguments for **L** ∥ $\hat{\mathbf{x}}$, **L** ∥ $\hat{\mathbf{y}}$, and **L** ∥ $\hat{\mathbf{z}}$ in Table I ($\hat{\cdot}$ denotes the Cartesian unit vector). Here, x and y refer to the zigzag and armchair directions of the Mn honeycomb sublattice, respectively. Our MAE calculations reveal that in-plane spin polarization (**L** ∥ $\hat{\mathbf{x}}$ and **L** ∥ $\hat{\mathbf{y}}$) is energetically more favorable than out-of-plane spin polarization (**L** ∥ $\hat{\mathbf{z}}$) by ∼0.5 meV per unit cell (or 0.023 μJ/cm^2), also tabulated in Table I. Note that the K and K' valleys are connected via $\mathcal{T}K = K'$ or $\mathcal{M}_xK = K'$. Hence, one can deduce that, when **L** ∥ $\hat{\mathbf{y}}$, the two valleys are degenerate. On the other hand, the valley degeneracy lifts for **L** ∥ $\hat{\mathbf{x}}$ (marginal) and **L** ∥ $\hat{\mathbf{z}}$ (band gaps differ by 64 meV at the two valleys). Our calculations can be seen in Fig. 1(d) for schematic plots and Fig. S1 in the Supplemental Material (SM) [45] for more details.

B. BPV effect and its valley dependence

Next, we show that the mirror reflection with respect to Néel vector **L** could lead to contrasting BPV photocurrent generation. We will focus on the LPL irradiation which, according to nonlinear optics theory, generates MIC in $\mathcal{PT}$-symmetric systems [46,47]. The current density is evaluated according to

$$\mathcal{J}^j = \eta_{ii}^j(0;\omega,-\omega)E^i(\omega)E^i(-\omega), \qquad (1)$$

where i and j refer to in-plane Cartesian axes (x or y), and **E**(ω) is the optical alternating electric field with the angular frequency ω. The MIC in $\mathcal{PT}$ systems can be viewed as a cousin effect to the normal injection current [35,46] which appears in nonmagnetic materials ($\mathcal{T}$-preserved and $\mathcal{P}$-broken) under circularly polarized light. It arises from the velocity difference between the valence and conduction bands, which increases linearly with time and saturates at the carrier relaxation time. According to band theory, its length-gauge form formula under long relaxation time limit is

$$\eta_{ii}^j(0;\omega,-\omega) = -\frac{\tau\pi e^3}{2\hbar^2}\int\frac{d^2\mathbf{k}}{(2\pi)^2}\sum_{mn}f_{mn}\Delta_{mn}^j g_{mn}^{ii}\delta(\omega_{mn}-\omega). \qquad (2)$$

Here, $f_{mn} = f_m - f_n$ and $\Delta_{mn}^j = v_{mm}^j - v_{nn}^j$ measure the Fermi-Dirac occupation and group velocity differences between the bands m and n, respectively. The Kronecker delta function $\delta(\omega_{mn}-\omega)$, represented by the Lorentz function with a broadening factor of 0.02 eV, guarantees the energy conservation law, with $\hbar\omega_{mn} = \hbar\omega_m - \hbar\omega_n$ referring to the eigenenergy difference. The MIC generation is scaled by quantum metric tensor $g_{mn}^{ii} = 2\sum_{\mu,\nu}\text{Re}(r_{m_\mu n_\nu}^i r_{n_\nu m_\mu}^i)$, where μ and ν represent the degenerate band indices, and the interband position matrix

is $r_{nm}^i = \langle n|\hat{r}^i|m\rangle = \frac{\langle n|\hat{v}^i|m\rangle}{i\omega_{gm}}$. All these quantities are **k** dependent which are omitted for clarity. The integral is performed in the whole 2D first BZ. We take an effective thickness as $d = 0.6$ nm, measured from its bulk counterpart. Then we divide the 2D photoconductivity [μA nm/V^2, according to Eq. (2)] by d, so that it adopts the conventional three-dimensional photoconductivity unit (μA/V^2).

It should be noted that there are two typical relaxation lifetimes controlling the injection current, namely, the intraband relaxation time τ_{intra} and the interband transition time τ_{inter}. According to previous works [48], the injection current photoconductivity linearly increases with time and saturates at τ_{intra}, which emerges in the coefficient before the integral in Eq. (2). On the other hand, the interband relaxation time τ_{inter} mainly enters the integrand in Eq. (2). Thus, we roughly estimate their effects individually (see Fig. S2 in the SM [45]). The η linearly increases with τ_{intra}, while it almost remains with respect to τ_{inter}. Rigorously speaking, the relaxation time depends on the band index n and momentum **k** as well as the environmental condition such as the temperature and the sample quality, e.g., disorder and impurity. Hence, a thorough and precise evaluation is not possible. In the following discussions, we follow the conventional approach to take a universal value (0.2 ps) that is usually adopted and is comparable with experimental observations [47,49]. This value can be approximately characterized by the electrical conductance according to the Drude model.

Before performing DFT calculations, we briefly analyze the magnetic point group for each case and its implication for BPV photocurrents. The highest symmetry arises when the Néel vector is parallel to z, **L** ∥ $\hat{\mathbf{z}}$, and the system belongs to magnetic point group $\bar{3}'m = C_{3v}\otimes\mathcal{PT}$. Since we are focusing on the MIC, which is invariant under $\mathcal{PT}$, we can use the C_{3v} point group (a character table can be found in Table S1 in the SM [45]) to conduct the symmetry analysis. For the electric field and current in the 2D (xy) plane, the irreducible representation for current and second-order symmetric field are $\Gamma_{\mathcal{J}} = E$ and $\Gamma_{(\mathbf{EE})^s} = A_1 \oplus E$. Hence, one has $\Gamma_{\mathcal{J}} \otimes \Gamma_{(\mathbf{EE})^s} = A_1 \oplus A_2 \oplus 2E$, allowing only one nonzero independent MIC component, which will be shown to be $\eta_{xx}^x = -\eta_{yy}^x = -\eta_{xy}^y$ and $\eta_{xx}^y = \eta_{yy}^y = \eta_{xy}^x = 0$. If we shift to the valley K (or K'), the C_{2y} rotation is broken (the little magnetic point group becomes $3m' = C_3 \oplus C_s\mathcal{T}$). Thus, the symmetry argument at each valley for MIC generation follows C_3, yielding $\Gamma_{\mathcal{J}} \otimes \Gamma_{(\mathbf{EE})^s} = E \otimes (A \oplus E) = 2A \oplus 2E$ with two allowed and independent MIC components (Table S2 in the SM [45]). This clearly indicates that momentum-dependent hidden MIC exists. This is akin to the hidden spin polarization (or spin Hall effect) as discovered locally in centrosymmetric ionic compounds and antiferroelectric materials [50–54], which arises in the real space due to the reduced symmetry constraints on each sector. Similar confinements can be found for the in-plane Néel vector, which breaks the threefold rotation $\mathcal{C}_{3z}$. The **L** ∥ $\hat{\mathbf{x}}$ belongs to $2'/m = \mathcal{C}_s \otimes \mathcal{PT}$, and the allowed MIC generation can be deduced from the C_s point group (Table S3 in the SM [45]). We then would have x-flowing MIC according to $\Gamma_{\mathcal{J}} \otimes \Gamma_{(\mathbf{EE})^s} = A' \otimes (2A' \oplus A'') = 2A' \oplus A''$. The two independent MICs would be η_{xx}^x and η_{yy}^x. The **L** ∥ $\hat{\mathbf{y}}$ is $2/m' = C_2 \otimes \mathcal{PT}$, and one can perform
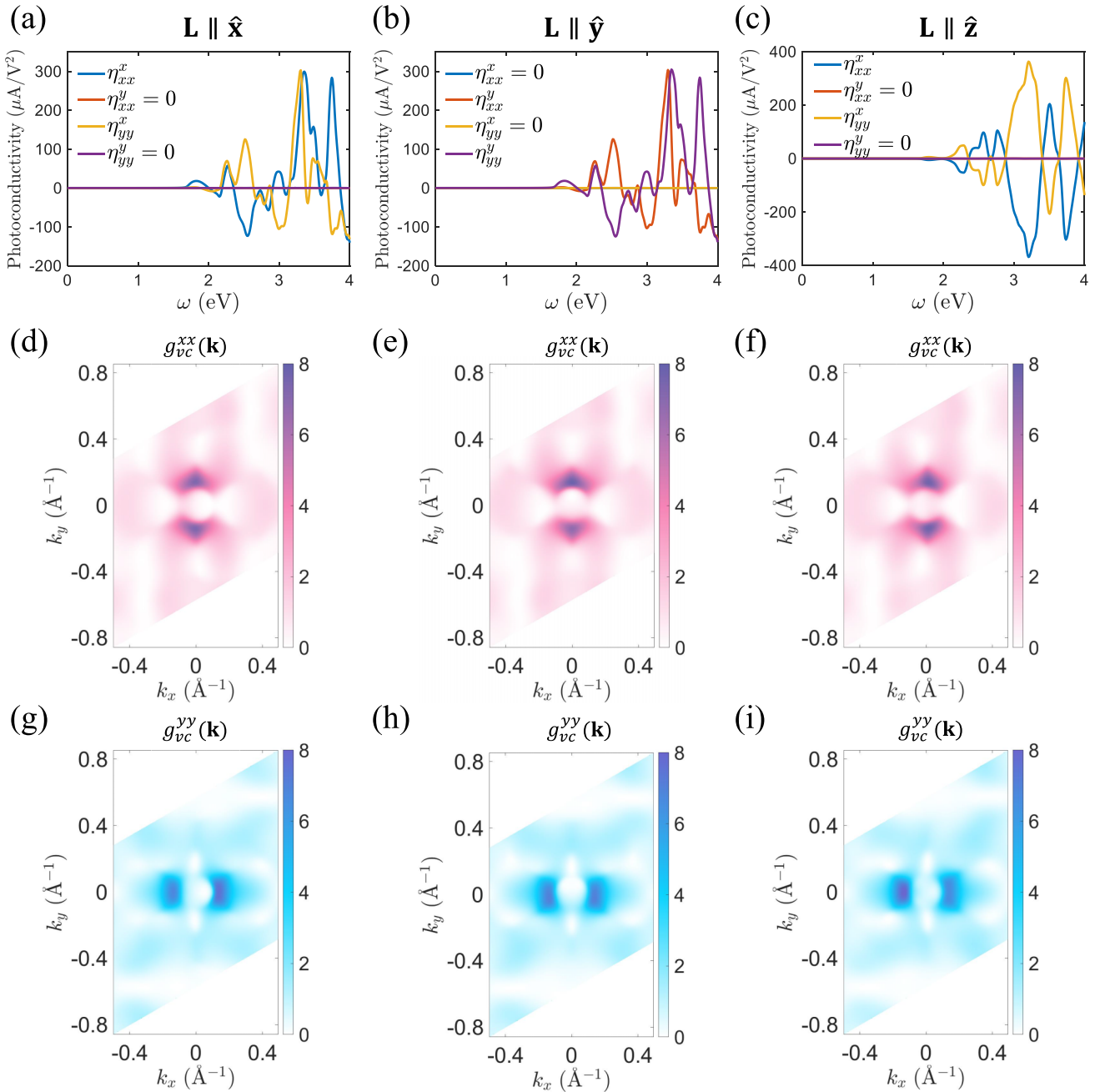
FIG. 2. Calculated magnetic injection current (MIC) photoconductivity under x- and y-polarized linearly polarized light (LPL) for (a) $\mathbf{L} \parallel \hat{\mathbf{x}}$, (b) $\mathbf{L} \parallel \hat{\mathbf{y}}$, and (c) $\mathbf{L} \parallel \hat{\mathbf{z}}$. In (c), we note that $\eta_{xx}^x(\omega) = -\eta_{yy}^x(\omega)$, arising from the C_{3z} rotation. Such symmetry is broken when $\mathbf{L}$ lies in-plane. Quantum metric distribution between the top valence and bottom conduction bands $g_{vc}^{xx}(\mathbf{k})$ over the first Brillouin zone (BZ) for (d) $\mathbf{L} \parallel \hat{\mathbf{x}}$, (e) $\mathbf{L} \parallel \hat{\mathbf{y}}$, and (f) $\mathbf{L} \parallel \hat{\mathbf{z}}$, and $g_{vc}^{yy}(\mathbf{k})$ for (g) $\mathbf{L} \parallel \hat{\mathbf{x}}$, (h) $\mathbf{L} \parallel \hat{\mathbf{y}}$, and (i) $\mathbf{L} \parallel \hat{\mathbf{z}}$ are also plotted.

similar arguments to yield the same results as in $\mathbf{L} \parallel \hat{\mathbf{y}}$. At the valleys, their 180°-rotation symmetry (2′ or 2) is no longer preserved. Hence, they both exhibit valley-dependent finite MIC components that are forbidden for the whole BZ due to local symmetry reduction.

The switching of $\mathbf{L}$ strongly affects the velocity texture distribution in $\mathbf{k}$-space, so that the MIC direction would depend on the Néel vector [see Eq. (2)]. In detail, when $\mathbf{L} \parallel \hat{\mathbf{x}}$ and $\mathbf{L} \parallel \hat{\mathbf{z}}$, the $\mathcal{M}_y$ reflection assigns $\mathcal{M}_y \Delta^y(k_x, k_y) = -\Delta^y(k_x, -k_y)$. On the contrary, for the $\mathbf{L} \parallel \hat{\mathbf{y}}$ case, we have $\mathcal{M}_y \mathcal{T} \Delta^x(k_x, k_y) = -\Delta^x(-k_x, k_y)$. Since the quantum metric

tensor is almost unchanged in these cases, one easily deduces that the x-flowing MIC is forbidden when $\mathbf{L} \parallel \hat{\mathbf{y}}$, while the y-flowing MIC is zero when $\mathbf{L} \parallel \hat{\mathbf{x}}$ or $\mathbf{L} \parallel \hat{\mathbf{z}}$. Note that, here, we assume the x (or y)-LPL. For a general polarization angle, such symmetry arguments may be changed, and the final MIC will be a component combination from the x-LPL and y-LPL.

Our first-principles calculations confirm the above qualitative analyses. In Figs. 2(a)–2(c), we plot the calculated total MIC generation. One clearly observes that $\eta_{ii}^y = 0$ for $\mathbf{L} \parallel \hat{\mathbf{x}}$ and $\mathbf{L} \parallel \hat{\mathbf{z}}$ ($i = x$ or y). When $\mathbf{L}$ is switched to along y, η_{ii}^x becomes zero. For the symmetrically allowed current, the
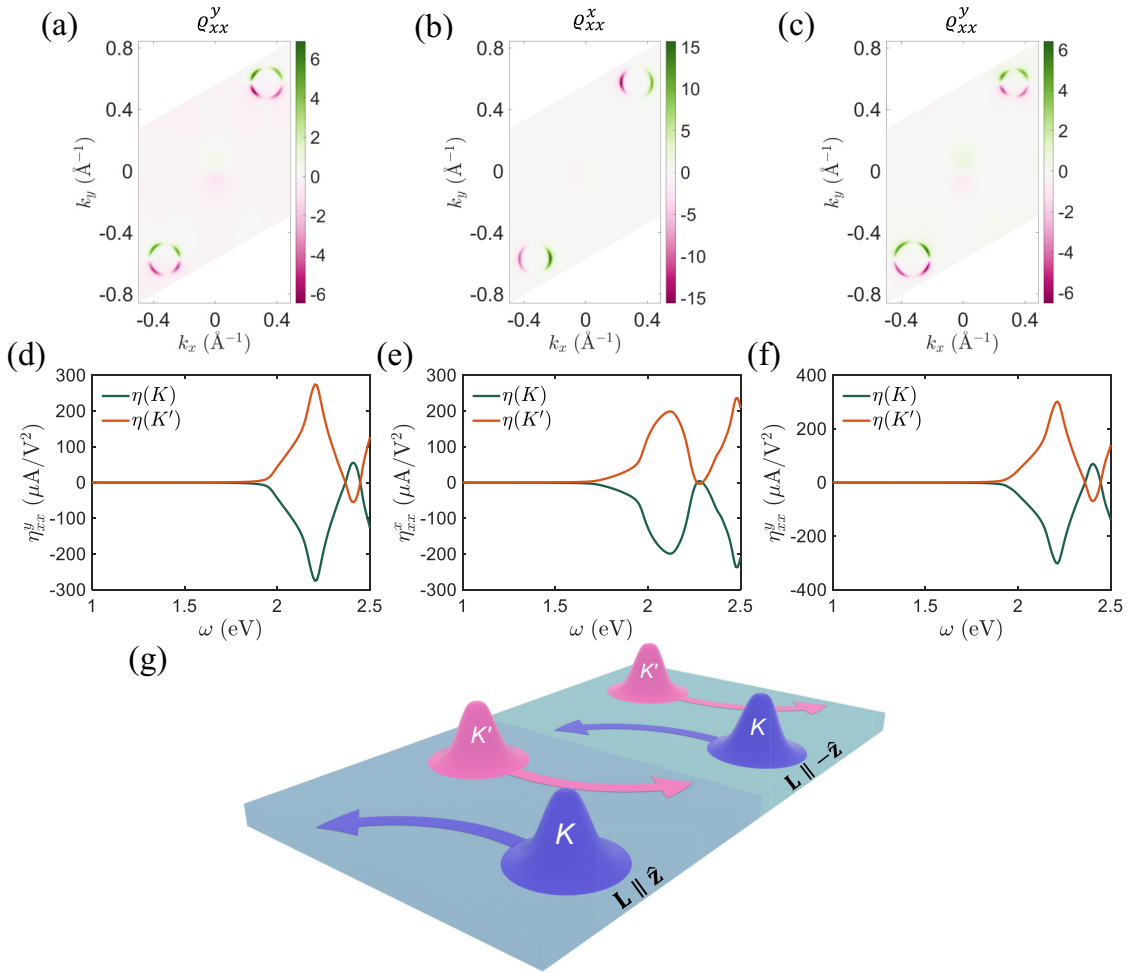
FIG. 3. Brillouin zone (BZ) contribution of magnetic injection current (MIC) integrand $\varrho_{xx}^{j}(\mathbf{k}, \omega) = \sum_{mn} f_{mn} \Delta_{mn}^{j} g_{mn}^{xx} \delta(\omega_{mn} - \omega)$ under x-linearly polarized light (LPL) irradiation for (a) $\mathbf{L} \parallel \hat{\mathbf{x}}$ ($j = y$), (b) $\mathbf{L} \parallel \hat{\mathbf{y}}$ ($j = x$), and (c) $\mathbf{L} \parallel \hat{\mathbf{z}}$ ($j = y$). Here, the incident photon energy is chosen to be $\hbar\omega = 1.8\,\text{eV}$ so that only near band edge states contribute to MIC. (d)–(f) plot their corresponding valley contrasting MIC contributions. (g) Schematic plot of magnetic heterostructure with two antiferromagnetic (AFM) configurations that are time-reversed with each other (e.g., between $\mathbf{L} \parallel \hat{\mathbf{z}}$ and $\mathbf{L} \parallel -\hat{\mathbf{z}}$). Valley-dependent bulk photovoltaic (BPV) current would accumulate at the two ends of the domain boundary.

magnitude of photoconductivity reaches $\sim 360\,\mu\text{A/V}^2$ ($\mathbf{L} \parallel \hat{\mathbf{z}}$). It indicates that, if we take the electric field magnitude of 0.1 MV/cm (at the photon energy of 3.2 eV or wavelength of 387 nm), corresponding to $1.3 \times 10^7\,\text{W/cm}^2$ light intensity, one could generate $\sim 3.6 \times 10^{-2}\,\mu\text{A/nm}^2$ current density. Across the lateral size of 1 nm (note that the effective thickness is $d = 6\,\text{Å}$), the current reaches $2.2 \times 10^{-2}\,\mu\text{A}$. Normal to this MIC, no net photocurrent can be detected. This vividly suggests that switching magnetic moment direction could drastically rotate the MIC generation direction. Such a large contrast can be directly measured via closed-circuit current or open-circuit voltage. The quantum metric between the top valence band and bottom conduction band (both doubly degenerate) $g_{vc}^{xx}(\mathbf{k})$ and $g_{vc}^{yy}(\mathbf{k})$ for $\mathbf{L} \parallel \hat{\mathbf{x}}$, $\mathbf{L} \parallel \hat{\mathbf{y}}$, and $\mathbf{L} \parallel \hat{\mathbf{z}}$ are shown in Figs. 2(d)–2(i). We can see the symmetry argument of $g_{vc}^{ii}(k_x, k_y) = g_{vc}^{ii}(k_x, -k_y)$, ($i = x$ or y) for $\mathcal{M}_y$ and $g_{vc}^{ii}(k_x, k_y) = g_{vc}^{ii}(-k_x, k_y)$ for $M_y \mathcal{T}$. In addition, we note that the time-reversal symmetry $\mathcal{T}$ that flips the Néel vector $\mathbf{L}$ (e.g., between $\mathbf{L} \parallel \hat{\mathbf{x}}$ and $\mathbf{L} \parallel -\hat{\mathbf{x}}$ or from $\mathbf{L} \parallel \hat{\mathbf{z}}$ to $\mathbf{L} \parallel -\hat{\mathbf{z}}$) also reverses the MIC generation while keeping the magnitude, as

η_{ii}^{j} is scaled by velocity operator and is $\mathcal{T}$ odd (see Fig. S3 in the SM [45]).

We then show that sizable valley-contrasting MIC emerges even when the net current is zero. To explicitly see this, we plot the $\mathbf{k}$-resolved MIC contributions, namely, the integrand of Eq. (2), for those symmetrically forbidden current components [Figs. 3(a)–3(c)]. The incident photon frequency is selected to be $\hbar\omega = 1.8\,\text{eV}$, slightly above the band gap. Their joint density of states can be seen in Figs. S4(a)–S4(c) in the SM [45], showing only band edge contributions. Even though the contributions around each valley show both positive and negative ridges, their summation is nonzero. In Figs. 3(d)–3(f), we plot the valley-dependent MIC, which is integrated around the valleys (within $\sim 0.3\,\text{Å}^{-1}$ near K/K'). We see that both valleys contribute significant MIC generation, reaching a photoconductivity of $\sim 300\,\mu\text{A/V}^2$. In each case, the MICs from the two valleys flow oppositely with the same magnitude, giving vanishing net MIC generation. A similar valley-dependent MIC also exists for the symmetrically allowed components (flowing along x), as plotted in Fig. S5 in
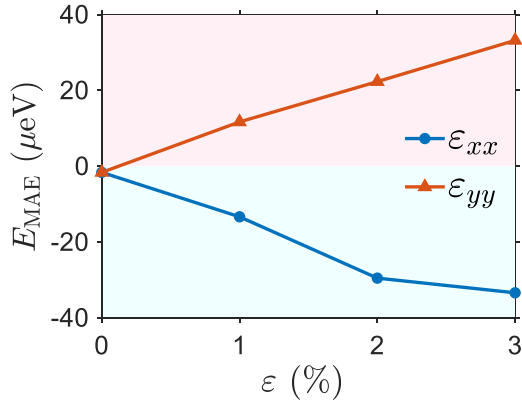
FIG. 4. Total energy difference (per unit cell) between $\mathbf{L} \parallel \hat{\mathbf{x}}$ and $\mathbf{L} \parallel \hat{\mathbf{y}}$ under uniaxial strain ε along x and y. The out-of-plane antiferromagnetic (AFM) configuration $\mathbf{L} \parallel \hat{\mathbf{z}}$ is always much higher in energy under such small strains.

FIG. 5. (a) Schematic plot of ferrotoroidicity in a rectangular supercell. Blue and red circles represent the antiparallel spin polarized Mn sites, and the two green circles (radius r_1 and r_2) are co-centered. Detailed explanation can be found in the main text. (b) Calculated magnetoelectric coefficient for $\mathbf{L} \parallel \hat{\mathbf{x}}$ and $\mathbf{L} \parallel \hat{\mathbf{y}}$. The abscissa axis denotes the chemical potential relative to the Fermi energy.

the SM [45]. The two valleys hold nearly oppositely flowing MIC, but they do not completely cancel each other.

This valley-contrasting BPV current has been largely overlooked previously and may find its potential applications in 2D valleytronic devices. We propose that this result implies another noncontacting scheme to generate valley currents, in addition to the electrically triggered (quantum) valley Hall effect. Experimentally, one could design a magnetic heterostructure [Fig. 3(g)] to separate and measure such a valley-dependent MIC. A valley contrasting MIC could accumulate at a domain wall between two AFM configurations, so that the current contributed from a specific valley K (or K') in both domains flow to their boundary. Note that this valley-contrasting current is different from the conventional valley Hall effect that has been well studied in nonmagnetic materials, where $\mathcal{T}$ symmetry constrains no net current with valley degeneracy. In the current case, the $\mathcal{PT}$ symmetry breaks the valley degeneracy (except when $\mathbf{L} \parallel \hat{\mathbf{y}}$). One could expect valley-dependent currents accumulated at the two ends of the boundary.

C. MAE modulation under strain

One may wonder how to harness the in-plane MAE ($E_{\mathrm{MAE}} = E_{\mathbf{L}\parallel\hat{\mathbf{x}}} - E_{\mathbf{L}\parallel\hat{\mathbf{y}}}$), so that Néel vector $\mathbf{L}$ can be pinned along x or y. We show that a uniaxial strain could further split the energy difference between $\mathbf{L} \parallel \hat{\mathbf{x}}$ and $\mathbf{L} \parallel \hat{\mathbf{y}}$. Our numerical results are shown in Fig. 4. At the equilibrium (strain-free) state, $\mathbf{L} \parallel \hat{\mathbf{x}}$ is almost degenerate with $\mathbf{L} \parallel \hat{\mathbf{y}}$ ($E_{\mathrm{MAE}} = -1.63 \, \mu\mathrm{eV}$ per unit cell). Under tensile strain along x (ε_{xx}), E_{MAE} reduces, so that Néel vector $\mathbf{L}$ prefers the x direction. On the other hand, the y-tensile strain increases E_{MAE}, aligning $\mathbf{L}$ along y. In both cases, a small strain of 3% (about elastic energy of 49 meV in 1 unit cell) could enhance the MAE magnitude to be $\sim 35 \, \mu\mathrm{eV}$ per unit cell, which is large enough to be distinguished in experiments. Furthermore, we find that such a small strain will not significantly alter the band structure in these cases, and the MIC photoconductivity marginally changes their values.

D. L-dependent ferrotoroidicity and magnetoelectric responses

In addition to the optically induced nonlinear current, we now show that the ferrotoroidicity is also sensitive to the Néel vector direction. Ferrotoroidicity has been discovered to be another primary ferroic order, compensating the ferroelasticity ($\mathcal{P}$-even, $\mathcal{T}$-even), ferroelectricity ($\mathcal{P}$-odd, $\mathcal{T}$-even), and ferromagnetism ($\mathcal{P}$-even, $\mathcal{T}$-odd) [55,56]. It reverses its sign under either $\mathcal{P}$ or $\mathcal{T}$ and is defined by the toroidal moment $\mathbf{t} = \sum_i \mathbf{r}_i \times \mathbf{s}_i$, where $\mathbf{r}_i$ and $\mathbf{s}_i$ represent the position and spin vectors of ion i, respectively, and the summation runs over all sites in the supercell. Previous theoretical and experimental works have disclosed a few ferrotoroidic bulk materials, such as $LiCoPO_4$ [57], $LiFeSi_2O_6$ [58], and defective $SrTiO_3$ [59]. Here, we suggest that the 2D $MnPSe_3$ monolayer also holds ferrotoroidic order with a sizable out-of-plane toroidal moment, if the Néel vector is pointing away from y. As shown in Fig. 5(a), we schematically depict the Mn sublattice distributions in a rectangular supercell which, without loss of generality, is uniaxially strained. The supercell contains four Mn sites, which locate on two co-centered circles with radii of r_1 and r_2. At the equilibrium state, these two green circles are identical, $r_1 = r_2$, and the angle $\theta = 30°$. Geometrically, if x-tensile strain is applied, θ reduces, and $r_1 < r_2$; y-tension will increase θ and makes $r_1 > r_2$.

We can directly estimate the toroidal moment $\mathbf{t}$ in this supercell setup. Note that, like the electric polarization $\mathbf{P}$, here, $\mathbf{t}$ is also multivalued with respect to a quanta, depending on the choice of origin. Nonetheless, we can use this position-spin cross-product definition to determine its existence. When the Mn spin polarization is along x, namely, $\mathbf{s} = (\pm s_x, 0, 0)$, it can be directly deduced that $\mathbf{t} = (0, 0, t_z)$ and $t_z = -\sum_{i=1}^4 y_i s_{i,x} = -2s_x(r_1 - r_2 \sin\theta) \neq 0$. Hence, it shows a nonzero toroidal moment along z. If $\mathbf{s} = (0, \pm s_y, 0)$, one could easily find $\mathbf{t} = (0, 0, 0)$, constrained by the $\mathcal{M}_y\mathcal{T}$ operation, even though the supercell is uniaxially strained. This can also be understood by analyzing the C_{2h} point group (Table S4 in the SM [45]). The $\mathbf{L} \parallel \hat{\mathbf{x}}$ belongs to the magnetic point group $2'/m$, giving a negative character for both C_2 rotation and inversion i. Hence, one has $\Gamma_m = B_u$ in which all other elements are represented by $+1$. The vertically aligned electric field and spin
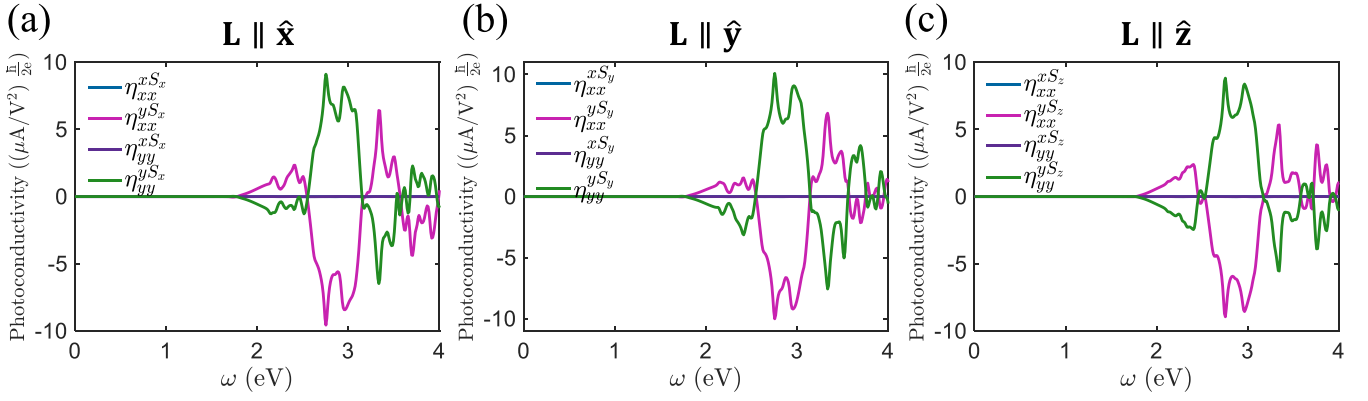
FIG. 6. Calculated bulk spin photovoltaic current photoconductivity under x- and y-polarized linearly polarized light (LPL): (a) $\mathbf{L} \parallel \hat{\mathbf{x}}$, (b) $\mathbf{L} \parallel \hat{\mathbf{y}}$, and (c) $\mathbf{L} \parallel \hat{\mathbf{z}}$.

polarization are presented by $\Gamma_{\mathbf{E}} = A_u$ and $\Gamma_{\mathbf{M}} = B_g$ (or $\Gamma_{\mathbf{E}} = B_u$ and $\Gamma_{\mathbf{M}} = A_g$), respectively. Then we have $\Gamma_m \otimes \Gamma_{\mathbf{E}} \otimes \Gamma_{\mathbf{M}} = A_g$ being symmetrically allowed. On the other hand, the magnetic point group of $2/m'$ for $\mathbf{L} \parallel \hat{\mathbf{y}}$ gives $\Gamma_m = B_g$. Thus, $\Gamma_m \otimes \Gamma_{\mathbf{E}} \otimes \Gamma_{\mathbf{M}} = A_u$, which is totally forbidden. Note that flipping Néel vector $\mathbf{L}$ corresponds to a time-reversal operation; thus, the ferrotoroidic vector $\mathbf{t}$ is also reversed between $\mathbf{L}$ and $-\mathbf{L}$.

The ferrotoroidicity can be reflected by the nondiagonal elements of magnetoelectric response coefficient tensor α^{EM}, defined as $M_j = \alpha^{\mathrm{EM}}_{ij} E_i$. According to Kubo perturbation theory, α^{EM} is calculated via

$$\alpha^{\mathrm{EM}}_{ij} = \frac{eA}{\hbar} \int \frac{d^2\mathbf{k}}{(2\pi)^2} \mathrm{Im} \sum_{n,l} \frac{f_{ln} v^i_{nl} m^j_{ln}}{(\omega_{ln} + i/\tau)^2}$$
$$+ \frac{eA}{\hbar} \tau \int \frac{d^2\mathbf{k}}{(2\pi)^2} \sum_n v^i_{nn} m^j_{nn} \delta(\omega_n - \mu). \quad (3)$$

Here, $m^j_{ln} = \langle l\mathbf{k}|\hat{m}^j|n\mathbf{k}\rangle \simeq -2\langle l\mathbf{k}|\hat{s}^j|n\mathbf{k}\rangle$ is the magnetic moment matrix element, and only spin contribution is considered in this work. Here, A refers to the area of unit cell; hence, $\alpha^{\mathrm{EM}}_{ij}$ measures the total spin contributed magnetic moments in the unit cell, induced by an in-plane static electric field E_i (also called the Rashba-Edelstein coefficient [60,61]). The first term arises from the Fermi sea contribution, while the second term evaluates the intrinsic contributions from the Fermi surface, being τ^1 dependent. According to previous discussions [62], $t_k \sim \epsilon_{ijk} \alpha^{\mathrm{EM}}_{ij}$, where ϵ_{ijk} is the Levi-Civita symbol (with Einstein summation convention). Thus, we plot the nondiagonal difference $(\alpha^{\mathrm{EM}}_{xy} - \alpha^{\mathrm{EM}}_{yx})$ as a function of chemical potential μ in Fig. 5(b). When $\mathbf{L} \parallel \hat{\mathbf{y}}$, $(\alpha^{\mathrm{EM}}_{xy} - \alpha^{\mathrm{EM}}_{yx}) = 0$, consistent with previous discussions. The $\mathbf{L} \parallel \hat{\mathbf{x}}$ pattern gives finite magnetoelectric responses. When the chemical potential lies inside the band gap, only extrinsic interband contribution exists, which is found to be $\sim 10^{-5}\,\mu_B\,\mathrm{nm/V}$ (μ_B is Bohr magneton). Upon n- or p-type doping, the intrinsic Fermi surface term jumps in, significantly increasing $(\alpha^{\mathrm{EM}}_{xy} - \alpha^{\mathrm{EM}}_{yx})$ to the order of $0.01\,\mu_B\,\mathrm{nm/V}$. Thus, an intermediate electric field with 0.1 V/nm strength yields $\sim 10^{-3}\,\mu_B$ magnetic moment variation, being sufficiently large for experimental observation. Considering the magnetic exchange parameter

J_{ex} of $0.12\,\mathrm{meV}/(\mu_B)^2$ in $\mathrm{MnPSe_3}$ [33], we can estimate the effective magnetic field of the magnetoelectric coupling to be ~ 0.02 Tesla per (V/nm). These magnetoelectric responses serve as an indirect and complementary demonstration for $\mathbf{L}$-dependent ferrotoroidicity.

IV. DISCUSSION

Before concluding, we would like to remark on a few points. In addition to charge current, recent advances have been extending the BPV effect into spin degrees of freedom, namely, bulk spin photovoltaic generation [47,63,64]. Previous works [35] have demonstrated that the LPL-induced spin photocurrent belongs to the shift current nature for $\mathcal{PT}$-symmetric systems, rather than the MIC mechanism for the electric charge current. The spin current operator is defined as $\hat{\mathbb{J}}^{ij} = \frac{1}{2}(\hat{v}^i \hat{s}^j + \hat{s}^j \hat{v}^i)$, where we adopt the spin polarization parallel to the Néel vector, namely, j is along $\mathbf{L}$. Our calculation results are plotted in Fig. 6. We find that no matter if $\mathbf{L}$ is parallel to x, y, or z, the spin currents always flow along y, making the x-propagating spin current symmetrically forbidden. This is because the spin current operator contains a surplus spin operator that transforms as a pseudovector. Also, the valley-dependent spin photocurrents still exist, though for the symmetrically forbidden spin current components.

The SOC effect plays an essential role in not only breaking the spin rotational symmetry but significantly affecting the
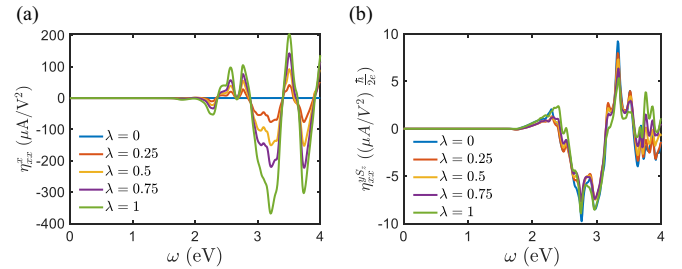
FIG. 7. (a) Magnetic injection current (MIC) photoconductivity η^x_{xx} and (b) spin current photoconductivity $\eta^{yS_z}_{xx}$ under $\mathbf{L} \parallel \hat{\mathbf{z}}$ when spin-orbit coupling (SOC) coefficient λ increases from 0 (SOC totally turned off) to 1 (full SOC is included). One sees that the charge current almost linearly increases with SOC effect, while the spin current is not largely affected.
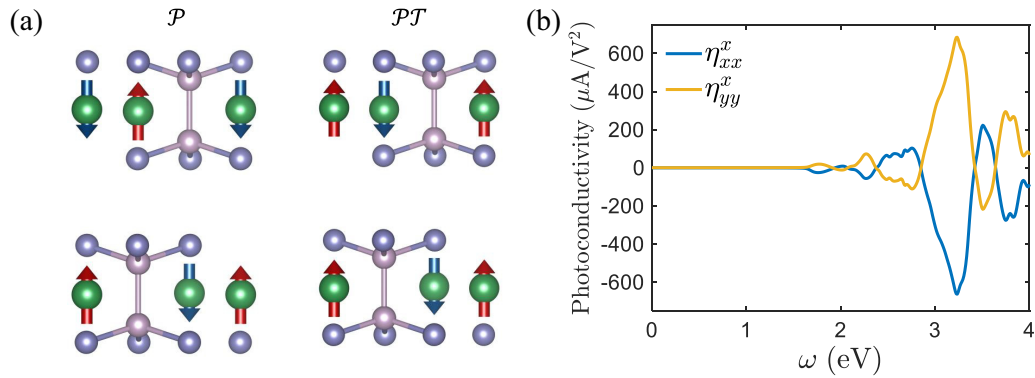
FIG. 8. (a) Bilayer MnPSe$_3$ structure in $\mathcal{P}$ and $\mathcal{PT}$ magnetic stacking patterns. They only differ in magnetic configurations of the upper layer, while the atomic coordinates are the same. (b) Magnetic injection current (MIC) of the $\mathbf{L} \parallel \hat{\mathbf{z}}$ in the $\mathcal{PT}$ magnetic pattern. The $\mathcal{P}$ magnetic pattern gives zero total bulk photovoltaic (BPV) photoconductivity.

MIC generation. To show this, we adjust the SOC strength by multiplying a tuning factor $\lambda \in [0, 1]$. Here, $\lambda = 0$ turns off the SOC effect, and $\lambda = 1$ refers to full SOC. As shown in Fig. 7, zero MIC is generated when the SOC is absent. We find that, as SOC is gradually increased, the symmetrically allowed MIC photoconductivity almost linearly enhances. Note that, when SOC is turned on, the spin magnetic quantum number is not conserved, and one cannot calculate the MIC from the two spin channels separately. Such SOC variation effects do not largely affect the spin current generation, which remains to be finite regardless with λ. We note that this SOC tunable BPV effect in AFM $\mathcal{PT}$-symmetric systems is different from the nonmagnetic ($\mathcal{T}$-symmetric, $\mathcal{P}$-broken) materials [47], where spin photocurrent linearly enhances with λ, but the electric charge current remains almost unchanged.

The AFM pattern also determines the symmetry constraints. In this paper, we focus on the Néel pattern in the MnPSe$_3$ monolayer, as determined by recent experiments [65,66]. If other transition metals are used, e.g., FePX_3 and CrPX_3 ($X =$ S or Se), a stripe or zigzag AFM pattern could become energetically optimal [31,33,67,68]. In those cases, the system is $\mathcal{P}$ symmetric rather than $\mathcal{PT}$. According to previous discussions, the second-order nonlinear BPV current totally vanishes, regardless of the local spin-polarization directions. In such circumstances, the band extrema in these cases do not locate at the K (or K') point; hence, it is unlikely to define and evaluate valley-polarized BPV effect, even though $\mathbf{k}$-resolved BPV photocurrents do not completely vanish.

Inversion symmetry could also preserve in Néel AFM patterns when we stack two monolayers together and form a MnPSe$_3$ bilayer. To illustrate this, we calculate the BPV photoconductivity, and the results are shown in Fig. 8. One could see that, depending on the spin-polarization patterns between the two monolayers, the whole system can be either $\mathcal{P}$ or $\mathcal{PT}$. Hence, zero or finite total photocurrent emerges in these cases.

This is akin to the recently proposed sliding ferroelectricity [69–71] that arises from atomic interfacial mismatch between the two layers, while here, it is the magnetic order that is mismatched at the interface. Such interlayer spin-order-adjusted symmetry in bilayer AFM materials is beyond the scope of this paper and will be discussed in detail elsewhere.

V. CONCLUSIONS

In summary, we conduct group theory analysis and first-principles calculations on the MnPSe$_3$ monolayer to show that photoinduced MIC generation in AFM $\mathcal{PT}$-symmetric materials sensitively depends on the spin-polarization Néel vector $\mathbf{L}$. The symmetry arguments, especially mirror reflection, vary by switching $\mathbf{L}$. In addition, we show that sizable valley-contrasting photocurrents could exist in AFM $\mathcal{PT}$-symmetric materials, even though the net MIC component is symmetrically constrained to be zero. The Néel vector direction can be well tuned by applying external uniaxial stress, which also harnesses the toroidal moment and the magnetoelectric coupling. In this paper, we provide an in-depth examination of the AFM magnetic order implications on various electrical and optical responses and pave the route to realizing nanoscale optoelectronic, optospintronic, and optovalleytronic devices with ultrafast kinetics.

[1] A. Rycerz, J. Tworzydło, and C. W. J. Beenakker, Valley filter and valley valve in graphene, Nature Phys. **3**, 172 (2007).

[2] D. Xiao, W. Yao, and Q. Niu, Valley-Contrasting Physics in Graphene: Magnetic Moment and Topological Transport, Phys. Rev. Lett. **99**, 236809 (2007).

[3] O. Gunawan, Y. P. Shkolnikov, K. Vakili, T. Gokmen, E. P. De Poortere, and M. Shayegan, Valley Susceptibility of an Interacting Two-Dimensional Electron System, Phys. Rev. Lett. **97**, 186404 (2006).

[4] J. Zhou, C. Huang, E. Kan, and P. Jena, Valley contrasting in epitaxial growth of In/Tl homoatomic monolayer with

anomalous Nernst conductance, Phys. Rev. B **94**, 035151 (2016).

[5] J. Li, K. Wang, K. J. McFaul, Z. Zern, Y. Ren, K. Watanabe, T. Taniguchi, Z. Qiao, and J. Zhu, Gate-controlled topological conducting channels in bilayer graphene, Nature Nanotech. **11**, 1060 (2016).

[6] H. Yu and W. Yao, Magnetization without polarization, Nature Mater. **16**, 876 (2017).

[7] F. Amet and G. Finkelstein, Could use a break, Nature Phys. **11**, 989 (2015).

[8] J. Zhou and P. Jena, Giant valley splitting and valley polarized plasmonics in group V transition-metal dichalcogenide monolayers, J. Phys. Chem. Lett **8**, 5764 (2017).

[9] T. Zhou, S. Cheng, M. Schleenvoigt, P. Schüffelgen, H. Jiang, Z. Yang, and I. Žutić, Quantum Spin-Valley Hall Kink States: From Concept to Materials Design, Phys. Rev. Lett. **127**, 116402 (2021).

[10] L. J. Sham, S. J. Allen, A. Kamgar, and D. C. Tsui, Valley-Valley Splitting in Inversion Layers on a High-Index Surface of Silicon, Phys. Rev. Lett. **40**, 472 (1978).

[11] F. J. Ohkawa and Y. Uemura, Theory of valley splitting in an N-Channel (100) inversion layer of Si I. formulation by extended zone effective mass theory, J. Phys. Soc. Jpn. **43**, 907 (1977).

[12] J. Zhou, Q. Sun, and P. Jena, Valley-Polarized Quantum Anomalous Hall Effect in Ferrimagnetic Honeycomb Lattices, Phys. Rev. Lett. **119**, 046403 (2017).

[13] Y. P. Shkolnikov, E. P. De Poortere, E. Tutuc, and M. Shayegan, Valley Splitting of AlAs Two-Dimensional Electrons in a Perpendicular Magnetic Field, Phys. Rev. Lett. **89**, 226805 (2002).

[14] D. Xiao, G.-B. Liu, W. Feng, X. Xu, and W. Yao, Coupled Spin and Valley Physics in Monolayers of MoS_2 and Other Group-VI Dichalcogenides, Phys. Rev. Lett. **108**, 196802 (2012).

[15] L.-J. Yin, H. Jiang, J.-B. Qiao, and L. He, Direct imaging of topological edge states at a bilayer graphene domain wall, Nat. Commun. **7**, 11760 (2016).

[16] L. Ju, Z. Shi, N. Nair, Y. Lv, C. Jin, J. Velasco, C. Ojeda-Aristizabal, H. A. Bechtel, M. C. Martin, A. Zettl et al., Topological valley transport at bilayer graphene domain walls, Nature (London) **520**, 650 (2015).

[17] T. Zhou, J. Zhang, H. Jiang, I. Žutić, and Z. Yang, Giant spin-valley polarization and multiple Hall effect in functionalized bismuth monolayers, npj Quantum Mater. **3**, 39 (2018).

[18] C. Chang, Y. Chen, Y. Chen, Y. Chen, F. Ding, C. Fan, H. J. Fan, Z. Fan, C. Gong, Y. Gong et al., Recent progress on two-dimensional materials, Acta Phys. -Chim. Sin. **37**, 2108017 (2021).

[19] X. Xu, Z. He, Y. Dai, B. Huang, and Y. Ma, Single-valley state in a two-dimensional antiferromagnetic lattice, Phys. Rev. B **104**, 205430 (2021).

[20] W.-Y. Tong, S.-J. Gong, X. Wan, and C.-G. Duan, Concepts of ferrovalley material and anomalous valley Hall effect, Nat. Commun. **7**, 13612 (2016).

[21] G. Xu, T. Zhou, B. Scharf, and I. Žutić, Optically Probing Tunable Band Topology in Atomic Monolayers, Phys. Rev. Lett. **125**, 157402 (2020).

[22] K. F. Mak, K. He, J. Shan, and T. F. Heinz, Control of valley polarization in monolayer MoS_2 by optical helicity, Nature Nanotech. **7**, 494 (2012).

[23] T. Cao, G. Wang, W. Han, H. Ye, C. Zhu, J. Shi, Q. Niu, P. Tan, E. Wang, B. Liu et al., Valley-selective circular dichroism

of monolayer molybdenum disulphide, Nat. Commun. **3**, 887 (2012).

[24] N. Ubrig, S. Jo, M. Philippi, D. Costanzo, H. Berger, A. B. Kuzmenko, and A. F. Morpurgo, Microscopic origin of the valley Hall effect in transition metal dichalcogenides revealed by wavelength-dependent mapping, Nano Lett. **17**, 5719 (2017).

[25] A. Gao, Y.-F. Liu, C. Hu, J.-X. Qiu, C. Tzschaschel, B. Ghosh, S.-C. Ho, D. Bérubé, R. Chen, H. Sun et al., Layer Hall effect in a 2D topological axion antiferromagnet, Nature (London) **595**, 521 (2021).

[26] T. Y. T. Hung, K. Y. Camsari, S. Zhang, P. Upadhyaya, and Z. Chen, Direct observation of valley-coupled topological current in MoS_2, Sci. Adv. **5**, eaau6478 (2019).

[27] Z. Wu, B. T. Zhou, X. Cai, P. Cheung, G.-B. Liu, M. Huang, J. Lin, T. Han, L. An, Y. Wang et al., Intrinsic valley Hall transport in atomically thin MoS_2, Nat. Commun. **10**, 611 (2019).

[28] T. Zhou, J. Zhang, B. Zhao, H. Zhang, and Z. Yang, Quantum spin-quantum anomalous Hall insulators and topological transitions in functionalized Sb(111) monolayers, Nano Lett. **15**, 5149 (2015).

[29] T. Zhou, J. Zhang, Y. Xue, B. Zhao, H. Zhang, H. Jiang, and Z. Yang, Quantum spin–quantum anomalous Hall effect with tunable edge states in Sb monolayer-based heterostructures, Phys. Rev. B **94**, 235449 (2016).

[30] V. M. Fridkin, Bulk photovoltaic effect in noncentrosymmetric crystals, Crystallogr. Rep. **46**, 654 (2001).

[31] B. L. Chittari, Y. Park, D. Lee, M. Han, A. H. MacDonald, E. Hwang, and J. Jung, Electronic and magnetic properties of single-layer MPX_3 metal phosphorous trichalcogenides, Phys. Rev. B **94**, 184428 (2016).

[32] A. J. Dekker, Ferromagnetism, antiferromagnetism, and ferrimagnetism, in *Solid State Physics* (Palgrave, London, 1981), pp. 464.

[33] N. Sivadas, M. W. Daniels, R. H. Swendsen, S. Okamoto, and D. Xiao, Magnetic ground state of semiconducting transition-metal trichalcogenide monolayers, Phys. Rev. B **91**, 235425 (2015).

[34] X. Li, T. Cao, Q. Niu, J. Shi, and J. Feng, Coupling the valley degree of freedom to antiferromagnetic order, Proc. Natl. Acad. Sci. USA **110**, 3738 (2013).

[35] H. Wang and X. Qian, Electrically and magnetically switchable nonlinear photocurrent in $\mathcal{PT}$-symmetric magnetic topological quantum materials, npj Comput. Mater. **6**, 199 (2020).

[36] G. Kresse and J. Furthmüller, Efficient iterative schemes for *ab initio* total-energy calculations using a plane-wave basis set, Phys. Rev. B **54**, 11169 (1996).

[37] G. Kresse and J. Furthmüller, Efficiency of *ab-initio* total energy calculations for metals and semiconductors using a plane-wave basis set, Comput. Mater. Sci. **6**, 15 (1996).

[38] J. P. Perdew, K. Burke, and M. Ernzerhof, Generalized Gradient Approximation Made Simple, Phys. Rev. Lett. **77**, 3865 (1996).

[39] P. E. Blöchl, Projector augmented-wave method, Phys. Rev. B **50**, 17953 (1994).

[40] H. J. Monkhorst and J. D. Pack, Special points for Brillouin-zone integrations, Phys. Rev. B **13**, 5188 (1976).

[41] V. I. Anisimov, J. Zaanen, and O. K. Andersen, Band theory and Mott insulators: Hubbard U instead of Stoner I, Phys. Rev. B **44**, 943 (1991).

[42] S. L. Dudarev, G. A. Botton, S. Y. Savrasov, C. J. Humphreys, and A. P. Sutton, Electron-energy-loss spectra and the structural

stability of nickel oxide: An LSDA+U study, Phys. Rev. B **57**, 1505 (1998).

[43] N. Marzari, A. A. Mostofi, J. R. Yates, I. Souza, and D. Vanderbilt, Maximally-localized Wannier functions: Theory and applications, Rev. Mod. Phys. **84**, 1419 (2012).

[44] X. Wang, J. R. Yates, I. Souza, and D. Vanderbilt, *Ab initio* calculation of the anomalous Hall conductivity by Wannier interpolation, Phys. Rev. B **74**, 195118 (2006).

[45] See Supplemental Material at http://link.aps.org/supplemental/10.1103/PhysRevB.107.245404 for character table for C_{3v}, C_3, C_s, and C_{2h} and the figures for band dispersion along the high symmetric **k**-path including influence of intraband relaxation time (τ_{intra}) and interband relaxation time (τ_{inter}) on the injection current photoconductivity η_{xx}^x, MIC photoconductivity under x- and y-polarized LPL, the jDOS at $\hbar\omega = 1.8\,\text{eV}$, and valley-dependent MIC photoconductivity under x-polarized LPL.

[46] H. Chen, M. Ye, N. Zou, B.-L. Gu, Y. Xu, and W. Duan, Basic formulation and first-principles implementation of nonlinear magneto-optical effects, Phys. Rev. B **105**, 075123 (2022).

[47] X. Mu, Y. Pan, and J. Zhou, Pure bulk orbital and spin photocurrent in two-dimensional ferroelectric materials, npj Comput. Mater. **7**, 61 (2021).

[48] Y. Shi and J. Zhou, Coherence control of directional nonlinear photocurrent in spatially symmetric systems, Phys. Rev. B **104**, 155146 (2021).

[49] B. M. Fregoso, Bulk photovoltaic effects in the presence of a static electric field, Phys. Rev. B **100**, 064301 (2019).

[50] X. Zhang, Q. Liu, J.-W. Luo, A. J. Freeman, and A. Zunger, Hidden spin polarization in inversion-symmetric bulk crystals, Nature Phys. **10**, 387 (2014).

[51] S. Guan and J.-W. Luo, Electrically switchable hidden spin polarization in antiferroelectric crystals, Phys. Rev. B **102**, 184104 (2020).

[52] H. Xu, J. Zhou, H. Wang, and J. Li, Light-induced static magnetization: Nonlinear Edelstein effect, Phys. Rev. B **103**, 205417 (2021).

[53] A. Johansson, B. Göbel, J. Henk, M. Bibes, and I. Mertig, Spin and orbital Edelstein effects in a two-dimensional electron gas: Theory and application to SrTiO$_3$ interfaces, Phys. Rev. Res. **3**, 013275 (2021).

[54] Y. Sun, X. Mu, Q. Xue, and J. Zhou, Tailoring photoinduced nonequilibrium magnetizations in In$_2$Se$_3$ bilayers, Adv. Opt. Mater. **10**, 2200428 (2022).

[55] A. S. Zimmermann, D. Meier, and M. Fiebig, Ferroic nature of magnetic toroidal order, Nat. Commun. **5**, 4796 (2014).

[56] J. Zhang, X. Wang, L. Zhou, G. Liu, D. Adroja, I. da Silva, F. Demmel, D. Khalyavin, J. Sannigrahi, H. Nair *et al.*, A ferrotoroidic candidate with well-separated spin chains, Adv. Mater. **34**, 2106728 (2022).

[57] B. B. Van Aken, J.-P. Rivera, H. Schmid, and M. Fiebig, Observation of ferrotoroidic domains, Nature (London) **449**, 702 (2007).

[58] P. Tolédano, M. Ackermann, L. Bohatý, P. Becker, T. Lorenz, N. Leo, and M. Fiebig, Primary ferrotoroidicity in antiferromagnets, Phys. Rev. B **92**, 094431 (2015).

[59] T. Shimada, Y. Ichiki, G. Fujimoto, L. Van Lich, T. Xu, J. Wang, and H. Hirakata, Ferrotoroidic polarons in antiferrodistortive SrTiO$_3$, Phys. Rev. B **101**, 214101 (2020).

[60] A. G. Aronov and Y. B. Lyanda-Geller, Nuclear electric resonance and orientation of carrier spins by an electric field, Pis'ma Zh. Eksp. Teor. fiz. **50**, 398 (1989) [JETP Lett. **50**, 431 (1989)].

[61] V. M. Edelstein, Spin polarization of conduction electrons induced by electric current in two-dimensional asymmetric electron systems, Solid State Commun. **73**, 233 (1990).

[62] N. A. Spaldin, M. Fiebig, and M. Mostovoy, The toroidal moment in condensed-matter physics and its relation to the magnetoelectric effect, J. Phys.: Condens. Matter **20**, 434203 (2008).

[63] H. Xu, H. Wang, J. Zhou, and J. Li, Pure spin photocurrent in non-centrosymmetric crystals: Bulk spin photovoltaic effect, Nat. Commun. **12**, 4330 (2021).

[64] K. Hamamoto, M. Ezawa, K.-w. Kim, T. Morimoto, and N. Nagaosa, Nonlinear spin current generation in noncentrosymmetric spin-orbit coupled systems, Phys. Rev. B **95**, 224430 (2017).

[65] Z. Ni, A. V. Haglund, H. Wang, B. Xu, C. Bernhard, D. G. Mandrus, X. Qian, E. J. Mele, C. L. Kane, and L. Wu, Imaging the Néel vector switching in the monolayer antiferromagnet MnPSe$_3$ with strain-controlled Ising order, Nature Nanotech. **16**, 782 (2021).

[66] A. Wiedenmann, J. Rossat-Mignod, A. Louisy, R. Brec, and J. Rouxel, Neutron diffraction study of the layered compounds MnPSe$_3$ and FePSe$_3$, Solid State Commun. **40**, 1067 (1981).

[67] J.-U. Lee, S. Lee, J. H. Ryoo, S. Kang, T. Y. Kim, P. Kim, C.-H. Park, J.-G. Park, and H. Cheong, Ising-type magnetic ordering in atomically thin FePS$_3$, Nano Lett. **16**, 7433 (2016).

[68] B. L. Chittari, D. Lee, N. Banerjee, A. H. MacDonald, E. Hwang, and J. Jung, Carrier- and strain-tunable intrinsic magnetism in two-dimensional MAX_3 transition metal chalcogenides, Phys. Rev. B **101**, 085415 (2020).

[69] M. Wu and J. Li, Sliding ferroelectricity in 2D van der Waals materials: Related physics and future opportunities, Proc. Natl. Acad. Sci. USA **118**, e2115703118 (2021).

[70] M. Wu, Two-dimensional van der Waals ferroelectrics: Scientific and technological opportunities, ACS Nano **15**, 9229 (2021).

[71] M. Vizner Stern, Y. Waschitz, W. Cao, I. Nevo, K. Watanabe, T. Taniguchi, E. Sela, M. Urbakh, O. Hod, and M. Ben Shalom, Interfacial ferroelectricity by van der Waals sliding, Science **372**, 1462 (2021).